Chemical Engineering Journal xxx (xxxx) xxx–xxx

Contents lists available at ScienceDirect

Chemical Engineering Journal

journal homepage: www.elsevier.com/locate/cej

Novel procedure for the numerical simulation of solar water disinfection processes in flow reactors

Ángela García-Gil, Cintia Casado, Cristina Pablos, Javier Marugán*

Department of Chemical and Environmental Technology, ESCET, Universidad Rey Juan Carlos, C/ Tulipán s/n, 28933 Móstoles, Madrid, Spain

HIGHLIGHTS

- Development of a numerical simulation model for SODIS processes in flow reactors.
- Coupling of solar vector calculation with radiation field resolution.
- Application of mechanistic kinetic model with explicit radiation absorption effect.
- Validation of the model in a tubular photoreactor coupled with a CPC reflector.
- Good prediction of experimental data under both simulated and natural sunlight.

GRAPHICAL ABSTRACT

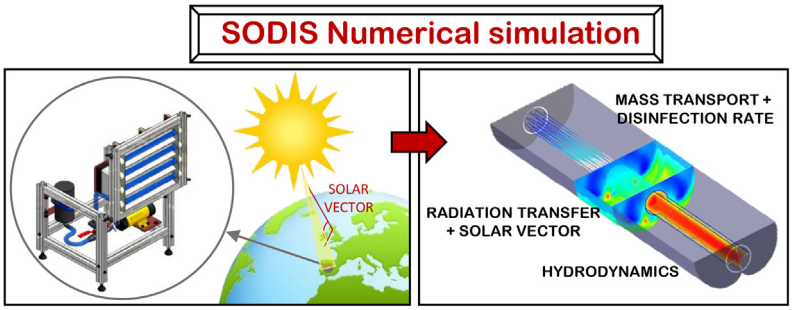

ARTICLE INFO

Keywords:
SODIS
Simulation
E. coli
CPC reactor
Solar vector
CFD

ABSTRACT

A novel procedure for the simulation of solar water disinfection (SODIS) processes in flow reactors is presented. The modeling approach includes the rigorous description of hydrodynamics, radiation transfer, mass transport and bacterial inactivation phenomena within the reactor by means of a computational fluid dynamics (CFD) software. The methodology has been evaluated in a tubular reactor coupled with a compound parabolic collector (CPC). Velocity profiles have been validated versus theoretical fully developed flow, and radiation fields versus both ray tracing and experimental actinometrical measurements. Incorporation of the solar vector calculation significantly improves the model capabilities for prediction of the potential performance of the SODIS process at different geographical coordinates and operation time. A mechanistic kinetic model was used for the description of the bacterial inactivation rate with explicit radiation absorption effects, coupling the radiation field with the mass balances of viable bacterial species. Model predictions successfully reproduce the experimental data of *E. coli* inactivation under different irradiances of both simulated and natural solar light with a normalized root mean squared logarithmic error (NRMSLE) of 6.65% and 9.72%, respectively. Therefore, this novel methodology is confirmed as a useful tool for the scaling-up of the SODIS process to large volume systems to be installed in remote communities where safe drinking water is not available.

1. Introduction

Solar disinfection (SODIS) process is a traditional water treatment method that can be used by communities where access to safe drinking water is a problem [1]. This process is usually carried out in PET (polyethylene terephthalate) bottles of 2 L that are exposed to sunlight radiation during 6 h under sunny days. SODIS process has been proved efficient for reducing water pathogens as bacteria, viruses, fungi or

* Corresponding author.
E-mail address: javier.marugan@urjc.es (J. Marugán).

https://doi.org/10.1016/j.cej.2018.10.131

protozoa [2]. However, it has some limitations, especially regarding the low capacity of the bottle based process, and the required exposure time of up to two days under cloudy conditions [3].

SODIS efficiency could be enhanced reducing the exposure time and increasing the production capacity by the use of photoreactors coupled with reflecting surfaces to collect the radiation instead of PET bottles. The most common configuration is the use of a tubular photoreactor coupled with a compound parabolic collector (CPC). This system has shown a high efficacy in comparison with the common PET bottles [4,5]. The acceptance angle of the collector is the most important factor in the geometrical design of the CPC [6]. Non-concentrating solar systems are able to collect diffuse and direct radiation of the sun [7], distributing homogeneously the solar radiation on the receptor. Therefore, an acceptance angle of 90°, corresponding to a concentration factor of 1 sun, is usually considered for the CPC design, so that all diffuse radiation can be captured [8,9]. Concentrating collector systems are able to increase the temperature, which is an advantage in the SODIS process. However, as the UV-A irradiance of the sunlight is the main factor in SODIS [10] and the fractions of direct and diffuse UV-A radiation received at sea level are similar, the use of non-concentrating collector systems is favorable for the SODIS process, especially in cloudy days when the radiation reaching the Earth surface is mostly diffuse.

Significant efforts have been devoted to the description of the physicochemical and biochemical phenomena taking place during SODIS. The process seems to be based on the formation of reactive oxygen species (ROS) upon absorption of UV-A photons by the nicotinamide adenine dinucleotide (NADH) present in living cells [11], and the simultaneous inactivation of the enzymes responsible for the control of the ROS levels. Although the most used disinfection kinetic models are empirical equations based on Chick's law [12], their lack of mechanistic base and explicit radiation absorption effects make them not suitable for the rigorous modeling and predictive simulation of the SODIS process. In contrast, Castro-Alférez et al. [13] developed a mechanistic kinetic model based on the photo-generation of internal ROS such as superoxide radical ($O_2^{\cdot-}$) and hydroxyl radical ($HO^{\cdot}$) and the photo-inactivation of the enzymes catalase (CAT) and superoxide dismutase (SOD) that successfully described the kinetics of the solar inactivation of *E. coli* in water. This microorganism, common indicator of faecal contamination, is the one usually employed to follow the efficiency of water disinfection processes.

Parallel efforts have being focused on the development of predictive methodologies for the simulation of photoreactors [14,15], as the use of photoreactors in water treatment applications has increased substantially over the past few years [16]. Computational fluid dynamics (CFD) has been previously applied to the simulation of water disinfection processes, such as ozonation [17] chlorination [18], and UV-C irradiation [19,20], but no previous studies on the CFD modeling of SODIS processes have been reported. On the other hand, CFD has been also applied to the study of CPC systems for energy and thermal applications [21–23]. Therefore, to the best of the authors' knowledge, there are no previous studies regarding the application of CFD modeling neither to the simulation of CPC systems for water treatment nor to the simulation of SODIS processes.

The present work reports a novel procedure for the CFD simulation of solar photoreactors for SODIS applications based on the rigorous description of the fluid dynamics, radiation transport, mass transfer and chemical reaction. The multiphysics approach is required due to the intrinsic photoactivated nature of the process, being the disinfection performance affected by the velocity profiles and radiation distribution in the reactor. Moreover, the calculation of the solar vector as a function of the geographic coordinates, date and time has been also included in the estimation of the theoretical solar irradiance received at the Earth surface. The model has been applied to a tubular photoreactor coupled to a CPC collector, being successfully validated with experimental data of *E. coli* inactivation.

2. Experimental methods

2.1. Photoreactor

The photoreactor setup consists on borosilicate tubes 26 mm in inner diameter and 380 mm in length (0.2 L of illuminated volume) located in the optical axis of a CPC aluminum reflector that provides 85% of direct light reflection towards the central pipe with a concentration factor of 1 sun [24]. Each tube operates in a closed recirculating circuit with a well-stirred reservoir tank of 1 L of total volume, being the water driven by a centrifugal pump with a flow rate of 12.12 $L \cdot min^{-1}$. The use of independent circuits makes possible carry out replicates under exactly the same experimental conditions. Two different light sources, simulated and natural sunlight, were used. Experiments with solar simulated light were carried out using a large scale solar simulator previously developed [24]. This system is based on a xenon lamp (Osram XBO 5000W/H XL) with a temperature color of 6000 K located on a cinema projector with a customized reflector to ensure the adequate homogeneous illumination of the CPC reflectors. Experiments under natural sunlight were carried out at Universidad Rey Juan Carlos facilities in Móstoles, Spain (40.33°N, 3.86°W), using a CPC inclination angle corresponding to the local latitude, as usually recommended for the optimal operation of CPC systems [5]. The irradiance at the *collection area* was measured by spectroradiometry using a *StellarNet Spectrometer UVIS-25* (329–400 nm) calibrated equipment. Potassium ferrioxalate actinometry experiments were carried out in order to calculate the total irradiation power for different emitted UV intensities as described elsewhere [25].

2.2. Bacterial inactivation experiments

E. coli K-12 (CECT 4624) strain was obtained from the Spanish Culture Collection (CECT) and used for experiments as model microorganism. Fresh liquid cultures were prepared by inoculation in Luria-Bertani (LB) nutrient medium and incubation at 37 °C with rotary shaking for 24 h until reaching a stationary concentration of around 10^9 $CFU \cdot mL^{-1}$. To prepare the reaction media, 5 mL of the liquid culture were centrifuged at 3000 rpm for 15 min. Bacteria was separated from supernatant, rinsed again with 5 mL of sterile saline solution (NaCl 0.9%), and diluted into the reactor tank to get an initial concentration in the range of 10^4–10^6 $CFU \cdot mL^{-1}$. Samples taken during the experiments were analyzed using the standard serial dilution method and plating in LB agar, being the colonies counted after incubation for 24 h at 37 °C.

Experiments were carried out in NaCl saline solution 0.9% w/v to avoid bacterial osmotic stress and they were conducted always in replicates. Temperature was kept below 35 °C during all experiments, ensuring no significant effect on the solar disinfection performance [2].

3. CFD model

3.1. Simulation procedure

The simulation model was developed and solved using the finite volume method implemented by ANSYS® Fluent v.14.5 (ANSYS Inc.). First, the solar photoreactor was geometrically defined in the computer assisted design (CAD) tool of the CFD software and optimally meshed considering the specific requirements of the variables and fields to be calculated. The simulation model is solved in three steps: i) flow field (equations of conservation of mass and momentum); ii) radiation field; and, iii) the conservation of species and chemical reactions (based on the previously calculated flow and radiation fields). The hydrodynamics and radiation field were simulated in steady state, whereas the bacterial inactivation process was solved in a transient state with 1 s time step, low enough to provide stable simulation results.

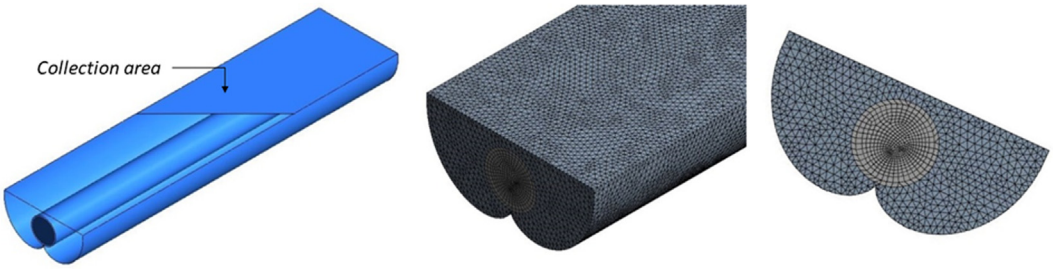

Fig. 1. Geometrical definition of the photoreactor and discretization mesh.

Table 1
Kinetic expressions of the main species involved in *E. coli* solar inactivation in water (adapted from [13]).

Step	Reaction rate	Units	Kinetic parameters
R1 – Bacterial inactivation	$r_{B_v} = k_{13}\cdot\frac{2\cdot\gamma_3[H_2O_2]_t}{k_6[H_2O_2]_t + k_{11}}\cdot\frac{\gamma_1+\gamma_2\cdot e^a_{NADH}}{k_3[SOD]_t + k_{12}}\cdot\{B_v\}_t$	$CFU\ mL^{-1}\ s^{-1}$	$k_3 = 10^9\ M^{-1}s^{-1}$ $k_6 = 2.7\cdot10^7\ M^{-1}s^{-1}$ $k_{11} = 2.04\cdot10^4\ s^{-1}$ $k_{12} = 1.36\cdot10^5\ s^{-1}$ $k_{13} = 8.03\cdot10^{15}\ M^{-2}s^{-1}$ $\gamma_1 = 5.4\cdot10^{-6}\ Ms^{-1}$ $\gamma_2 = 1.14\cdot10^5\ M\ cm^3\ Einstein^{-1}$
R2 – H_2O_2 decomposition	$r_{H_2O_2} = \frac{1}{2}\cdot\frac{k_3[SOD]_t(\gamma_1+\gamma_2\cdot e^a_{NADH})}{k_3[SOD]_t + k_{12}}\cdot\frac{\gamma_3 k_6[H_2O_2]_t^2}{k_{11}+k_6[H_2O_2]_t} - (\gamma_3 + k_8[CAT]_t)[H_2O_2]_t$	$M\ s^{-1}$	$k_8 = 9\cdot10^5\ M^{-1}s^{-1}$ $\gamma_3 = 1.4\cdot10^{-3}\ s^{-1}$
R3 – CAT inactivation	$r_{CAT} = k_9\cdot e^a_{CAT}\cdot[CAT]_t^2$	$M\ s^{-1}$	$k_9 = 1.5\cdot10^7\ cm^3\ Einstein^{-1}$
R4 – SOD inactivation	$r_{SOD} = k_{10}\cdot e^a_{SOD}\cdot[SOD]_t^2$	$M\ s^{-1}$	$k_{10} = 1.56\cdot10^6\ cm^3\ Einstein^{-1}$

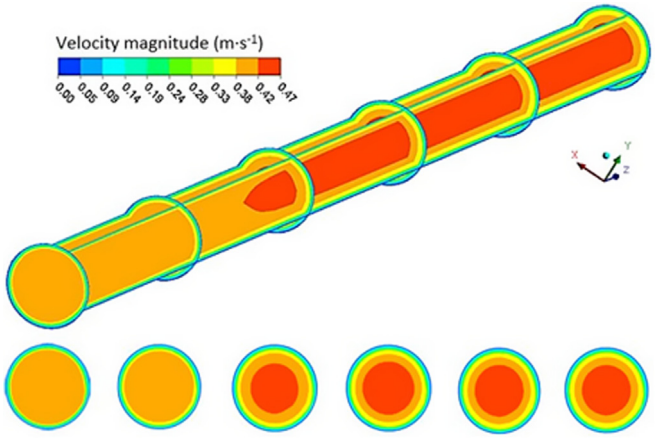

Fig. 2. Velocity field along the tubular reactor and cross sections at increasing distances from the inlet of 0, 7.56, 15.1, 22.7, 30.3 and 38 cm (outlet).

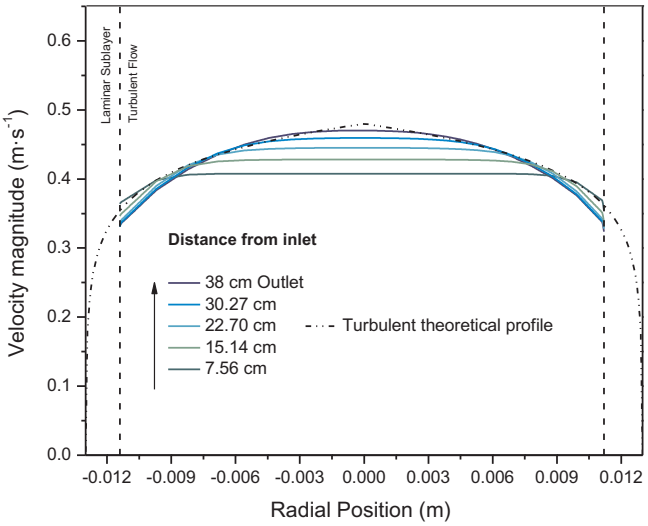

Fig. 3. Comparison of the velocity profile calculated by the simulation and the theoretical profile of fully developed turbulent flow.

3.2. Geometry and mesh of the photoreactor

The geometrical model of the system was defined using the ANSYS® Workbench tool (Fig. 1) and includes the tubular photoreactor and the CPC reflector. Tank and pipes were not drawn, being the recirculation effect included by a *user defined function* (UDF). A boundary condition was set in the *collection area* to transmit the homogeneous radiation received from the light source. An air domain was defined between the *collection area*, the reflector surface and the tubular reactor to allow the calculation of the radiation transport. All the reactor volume considered was meshed with approximately 600,000 volumetric cells using ANSYS® meshing tool. The number of cells was determined to be high enough to provide mesh independent simulation results of the global incident radiation and net radiation fluxes below 10^{-6}.

3.3. Hydrodynamics and mass transfer

The solution of the flow field was computed by solving the continuity equation and the Navier-Stokes equations for steady state (Eqs. (1) and (2)):

$$\nabla\cdot(\rho\bar{v}) = 0 \quad (1)$$

$$\rho\nabla\cdot(\rho\bar{v}\bar{v}) = -\nabla P + \nabla\cdot\bar{\tau} + \rho\vec{g} \quad (2)$$

where ρ, $\bar{v}$, P, $\bar{\tau}$ y $\vec{g}$ are the density, velocity vector, pressure, stress tensor due to molecular viscosity and the gravity acceleration.

Steady state and turbulent flow (the Reynolds number is 10,140) were applied. The fluids were assumed to be Newtonian,

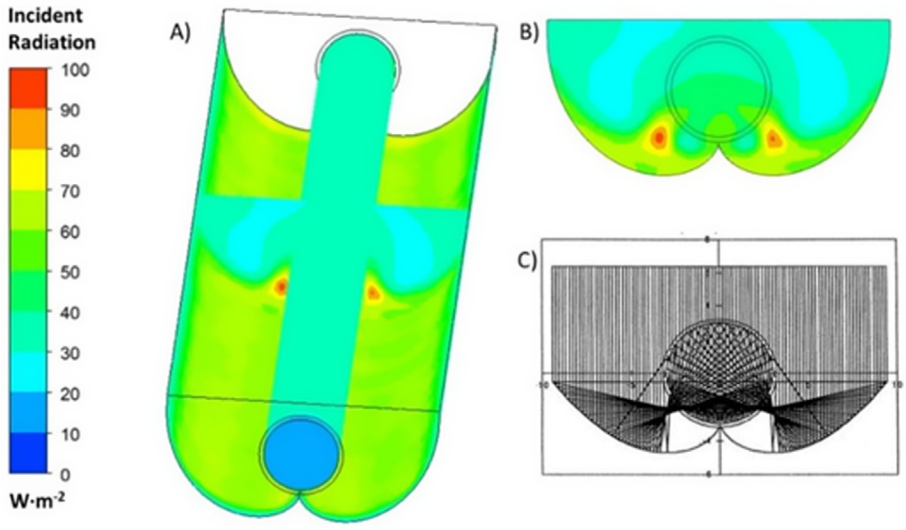

Fig. 4. A) Light distribution in the photoreactor and CPC for a UV irradiance of 16.4 $W{\cdot}m^{-2}$ perpendicular to the *collection area*. B) Cross section of the central plane of the reactor. C) Radiation distribution calculated by Robert & Malato [38].

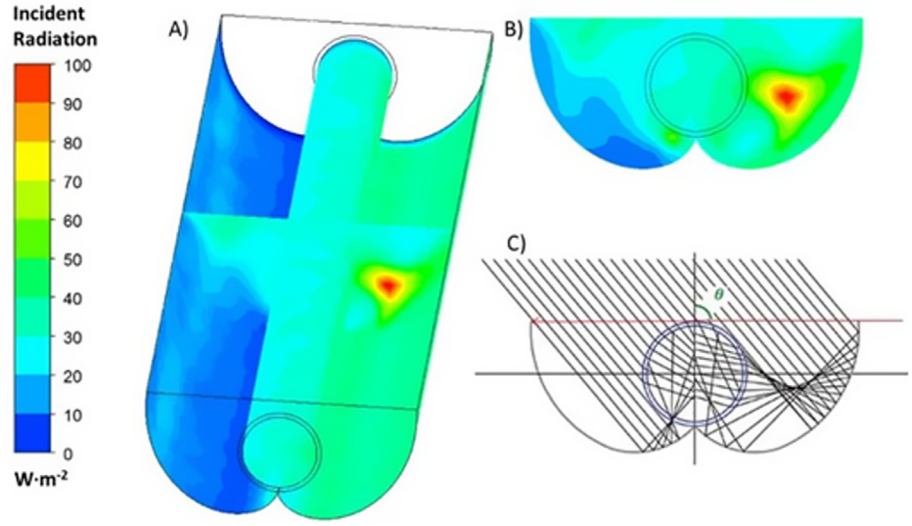

Fig. 5. A) Light distribution in the photoreactor and CPC for a UV irradiance of 16.4 $W{\cdot}m^{-2}$ angled 45° with respect to the *collection area*. B) Cross section of the central plane of the reactor, C) Distribution of radiation in a CPC with an acceptance angle of 180° [39].

Table 2
Comparison of the incident radiation in the photoreactor predicted by the model based on the radiometric irradiance values measured in the *collection area* and the experimental actinometrical data using solar simulated light.

Irradiance in the *collection area* ($W{\cdot}m^{-2}$)	Incident radiation in the reactor ($W{\cdot}m^{-2}$)	
	Simulation	Actinometry
14.9	40.04	42.54 ± 2.13
18.6	50.09	50.42 ± 2.52
22.1	59.39	57.77 ± 2.89

incompressible and isothermal with constant physical properties. The inlet velocity was set to 0.39 $m{\cdot}s^{-1}$ (12.12 $L{\cdot}min^{-1}$) and atmospheric pressure was considered at the outlet.

The semi-empirical standard k-ε model was selected for turbulence calculation. It is used for completely turbulent regimes by the following transport equations (Eqs. (3) and (4)):

$$\frac{\partial}{\partial t}(\rho k) + \frac{\partial}{\partial x_i}(\rho k u_i) = \frac{\partial}{\partial x_j}\left[\left(\mu + \frac{\mu_t}{\sigma_k}\right)\frac{\partial k}{\partial x_j}\right] + G_k + G_b - \rho\varepsilon - Y_M + S_k \tag{3}$$

$$\frac{\partial}{\partial t}(\rho \varepsilon) + \frac{\partial}{\partial x_i}(\rho \varepsilon u_i) = \frac{\partial}{\partial x_j}\left[\left(\mu + \frac{\mu_t}{\sigma_\varepsilon}\right)\frac{\partial \varepsilon}{\partial x_j}\right] + C_{1\varepsilon}\frac{\varepsilon}{k}(G_k + C_{3\varepsilon}G_b) - C_{2\varepsilon}\rho\frac{\varepsilon^2}{k} + S_\varepsilon \tag{4}$$

These expressions calculate turbulence kinetic energy (k) and its rate of dissipation (ε). G_k is the generation of turbulence kinetic energy due to the mean velocity gradients; G_b the generation of turbulent kinetic energy due to buoyancy; ρ the density; Y_M the contribution of the fluctuating dilatation in compressible turbulence to the overall dissipation; $C_{1\varepsilon}$, $C_{2\varepsilon}$ and $C_{3\varepsilon}$ constants values are obtained from literature [26]; and σ_ε and σ_k Prandtl numbers for ε and k. S_k and S_ε are user-defined source terms, if needed.

The turbulence level is assessed by the hydraulic diameter (d_h) and turbulence intensity (I). The turbulence intensity can be estimated using the equation (Eq. (5)). In this reactor, 5% turbulence intensity was calculated, in agreement with the typical value recommended for

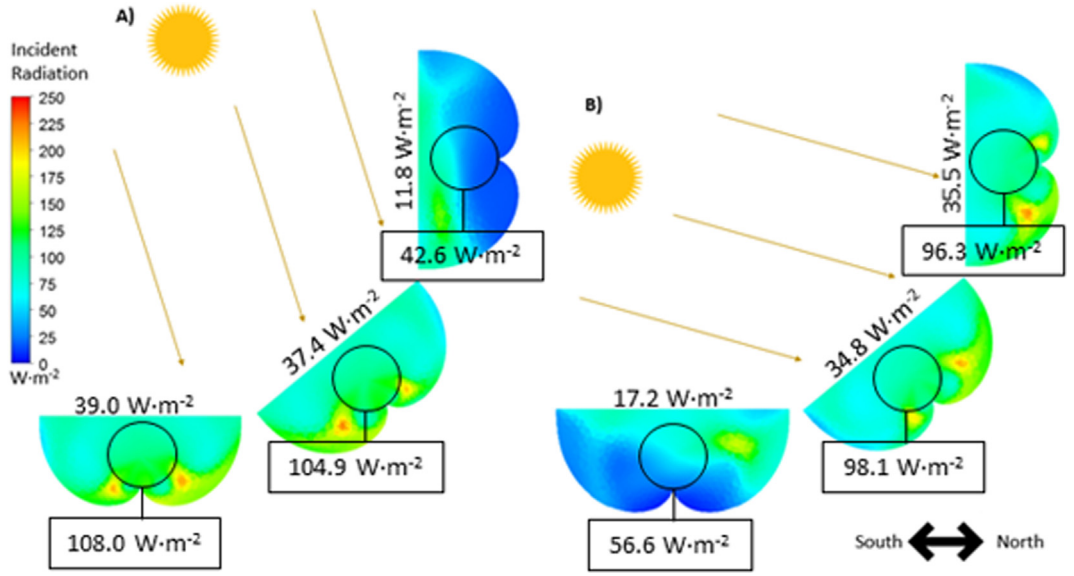

Fig. 6. Solar UV irradiation incident over the central plane of the reactor for different inclinations of the CPC (horizontal, vertical and facing to the Equator with an angle de 40° corresponding to the local latitude of Móstoles, (Spain) in the solar noon of the winter and summer solstice.

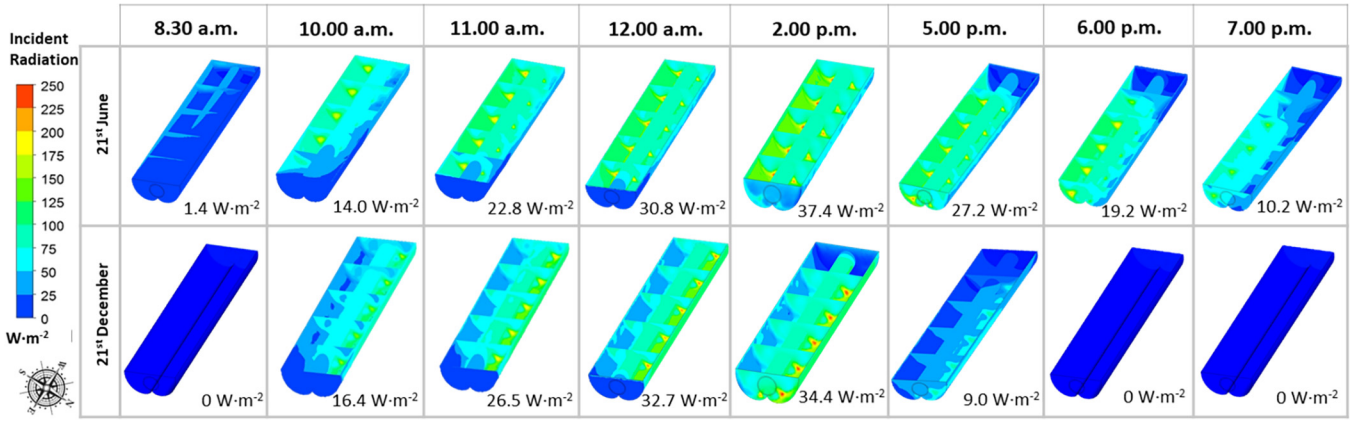

Fig. 7. UV incident radiation in the reactor, on 21st June and 21st December at different hours of the day with an angle de 40° corresponding to the local latitude of Móstoles (Spain).

cylindrical pipes [27].

$$I = 0.16 \cdot Re_{d_h}^{-\frac{1}{8}} \tag{5}$$

3.4. Radiation model

The rigorous modeling of the radiation field in the photoreactor requires the solution of the *radiative transfer equation* (RTE) (Eq. (6)):

$$\frac{dI(\vec{r},\vec{s})}{ds} + (\kappa + \sigma_s)\cdot I(\vec{r},\vec{s}) = \kappa \cdot n^2 \cdot \frac{\sigma \cdot T^4}{\pi} + \frac{\sigma_s}{4\pi} \cdot \int_0^{4\pi} I(\vec{r},\vec{s}')\cdot\Phi(\vec{s}\cdot\vec{s}')d\Omega \tag{6}$$

where $\vec{r}$ and $\vec{s}$ are position and direction vector, s the path length, I the radiation intensity, κ and σ_s are the absorption and scattering coefficients, n the refraction index, σ the Stefan-Boltzmann constant ($5.669 \cdot 10^{-8}\,W \cdot m^{-2} \cdot K^{-4}$), and T the local temperature. Φ is the phase function that describes the scattering phenomenon.

The numerical solution of this equation can be obtained by the *discrete ordinate method* (DOM). This method solves the radiation field at any point inside the geometry for a finite number of discrete solid angles, each one associated with a direction vector. When the DOM is used, the spatial discretization is taken from the mesh grid topology, but a directional discretization is also required. An angular discretization of the sphere octant of 15 × 15 divisions and 1 × 1 pixels was specified to avoid the "ray effect" and angle overhanging respectively.

All the model surfaces were set as semi-transparent and zero-thickness. A specular reflectivity of the 85% was defined for the reflector surface. The water (bacterial suspension) was considered as a homogenous medium. As the emission of radiation can be neglected at the low operation temperatures of the process, the temperature was fixed to 1 K in all domains to inactivate calculations of radiation emission.

As it will be shown below, for bacterial inactivation purposes, radiation can be considered to be absorbed by CAT and SOD enzymes and NADH. The specific absorption coefficients (κ^*) were obtained from the literature, using an average value in the UV-A range (300–400 nm): κ^*_{CAT} as $2.6 \cdot 10^5\,M^{-1} \cdot cm^{-1}$ [13]; κ^*_{SOD} as $800\,M^{-1} \cdot cm^{-1}$ [28]; and κ^*_{NADH} as $6220\,M^{-1} \cdot cm^{-1}$ [29]. The volumetric absorption coefficients (κ) were calculated (in cm^{-1}) by multiplying the corresponding specific values by the molar concentration of the compound i (Eq. (7)).

$$\bar{\kappa}_i = \bar{\kappa}_i^* \cdot [i] \tag{7}$$

The concentration of NADH, CAT and SOD species used in the kinetic model are referred to the bacterial cell volume. Therefore, these values have to be multiplied by the concentration of bacteria in water

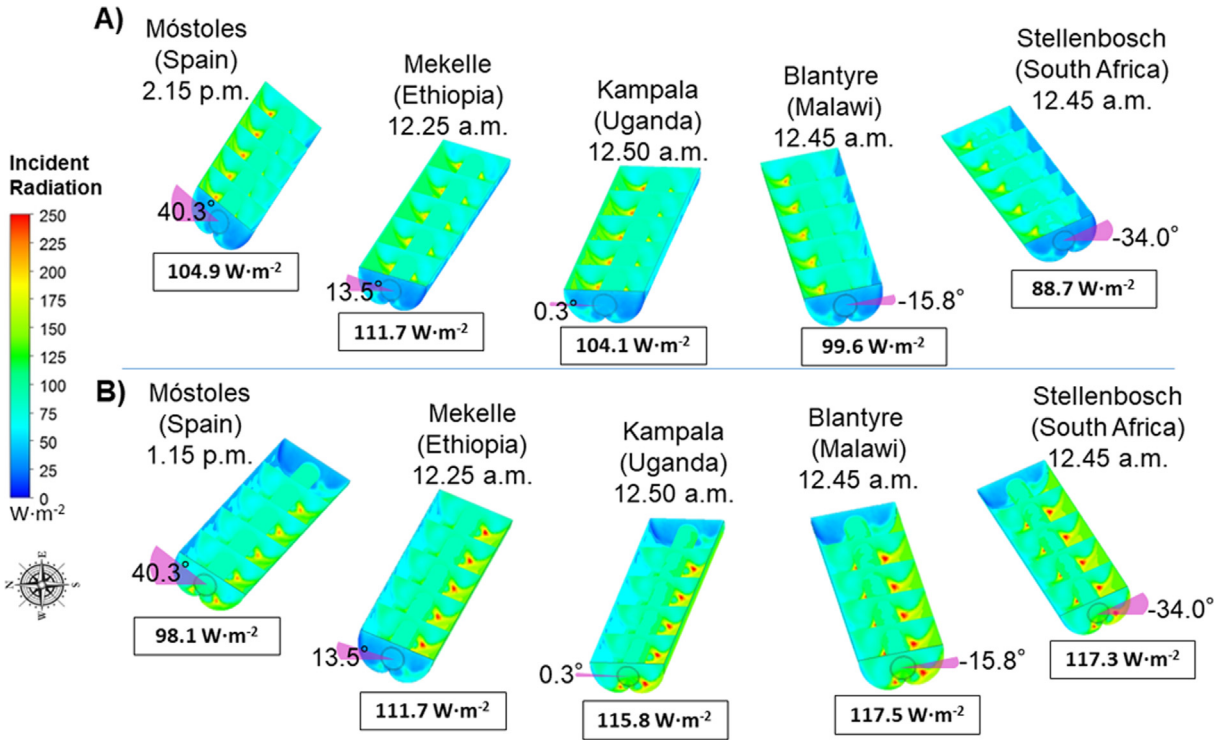

Fig. 8. Average UV incident radiation in the photoreactor at selected locations on the Earth's surface: A) 21st June and B) 21st December. All the simulations conducted at the solar noon with the CPC facing the Equator with an inclination angle corresponding to the local latitude.

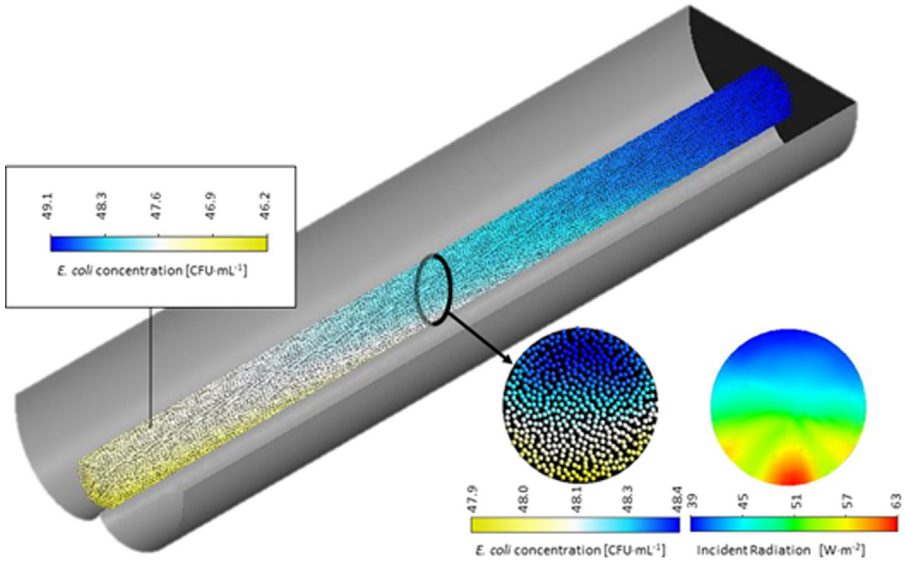

Fig. 9. Example of the distribution of viable *E. coli* bacteria along the photoreactor in a certain time step (irradiation time of 2000 s; initial concentration of E. coli of 10^6 CFU·mL^{-1} ; irradiance of 15.7 W·m^{-2}).

and the ratio between the bacterial volume and the total water volume assuming a typical size of *E. coli* bacteria of 1 μm in length and 0.5 μm in diameter ($1.96{\cdot}10^{-13}$ cm^3). Assuming a constant NADH concentration at the basal *E. coli* concentration of $2.5{\cdot}10^{-4}$ M [30], and initial concentrations of CAT and SOD in the cell of $9.2{\cdot}10^{-5}$ M [31,32] and $2{\cdot}10^{-5}$ M [33], the maximum values of the absorption coefficients of these species in the whole reactor volume can be estimated as $3.05{\cdot}10^{-7}$ cm^{-1}, $4.68{\cdot}10^{-6}$ cm^{-1} and $3.19{\cdot}10^{-9}$ cm^{-1} for NADH, CAT and SOD, respectively. These values can be considered low enough to neglect absorption effects by these species in the calculation of the radiation distribution, being solved the intensity field in steady state. The values of the local volumetric rate of photon absorption (LVRPA, e^a) for NADH, CAT and SOD can be estimated by multiplying the values of the calculated incident radiation by the corresponding absorption coefficients.

3.4.1. Simulated solar light

Due to the unnecessary high computational cost of the simulation of the radiation transport from the xenon lamp to the photoreactor and CPC reflector, the UV incident radiation was provided as a boundary condition at the *collection area*, with emission values of 15.7, 21.7 and 24.8 W·m^{-2} and a direction perpendicular to the collection surface.

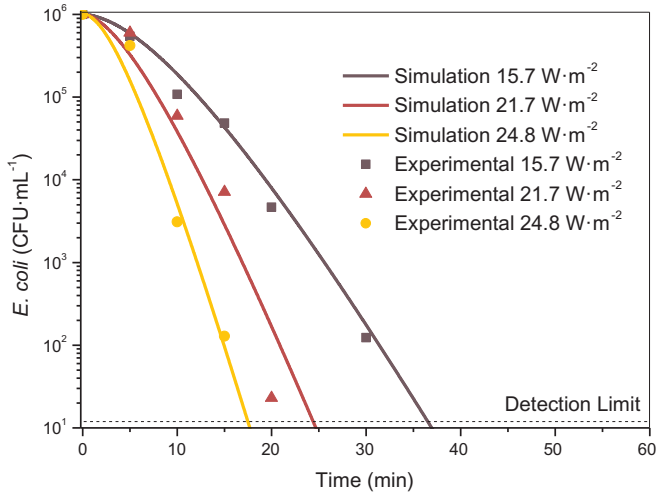

Fig. 10. Comparison of the results of the SODIS modelling and the experimental data for *E. coli* inactivation under simulated solar light.

3.4.2. Natural sunlight

The intensity and direction of the incident solar radiation was estimated using the *solar calculator* tool of ANSYS® Fluent. This tool calculate the solar vector using an algorithm from the National Renewable Energy Laboratory (NREL, USA) database [34], allowing the definition of the direction of the incident radiation in the *collection area* of the CPC and its coupling as boundary conditions to the DOM solution. Regarding the calculation of the irradiance, the *solar calculator* offers two different ways: *theoretical maximum* or *fair weather conditions* (FWC) model [35]. In this work, the FWC model was selected because it considers a more realistic attenuation of solar radiation in the atmosphere. Additionally, a cloudiness factor ranging from 0 to 1 can be added to correct the estimated value of the radiation intensity. The total irradiance provided by the solar calculator tool corresponds to the whole spectrum of the solar light. Therefore, only 4.1% of the total irradiance was considered as UV radiation input, being this percentage established based on the UV fraction of the solar spectrum ASTM G-173 AM1.5 standard [36].

3.5. Chemical reaction

Finally, as a transient process, the CFD simulation of the chemical reaction requires the solution of the mass balance of each species in a non-stationary state including not only mass transfer by diffusion and advection mechanisms, but also the chemical reaction term. For each individual chemical compound *i* in the computational domain, the mass conservation equation can be expressed as the equation (Eq. (8)):

$$\frac{\partial}{\partial t}(\rho Y_i) + \nabla\cdot(\rho\bar{v}Y_i) = \nabla J_i + R_i \tag{8}$$

where Y_i is the mass fraction of *i* in the mixture; J_i is its diffusive flux; and R_i its rate of production. The velocity vector, $\bar{v}$, couples the mass balances to the hydrodynamics calculations. The diffusive flux can be estimated using Fick's first law of diffusion (Eq. (9)):

$$J_i = -\rho D_{i,m}\nabla Y_i \tag{9}$$

The *E. coli* diffusion coefficient was established as $9.2{\cdot}10^{-7}$ $cm^2{\cdot}s^{-1}$ [37].

The chemical reaction term (R_i) must be calculated from a kinetic model which includes the energy absorption term, as SODIS is a photoactivated process. As ANSYS® Fluent only incorporates kinetic models of thermo-activated reactions, it was required to include the reaction rate of each species as a function of the local volumetric rate of photon absorption through developed programming code in a UDF.

A mechanistic model of solar SODIS processes was used to describe the inactivation of *E. coli* along the illumination time. Table 1 shows the reaction rate expression and the values of the kinetic parameters obtained from the literature (details of the kinetic model can be found elsewhere [13]).

The reactor performance was simulated for different values of irradiation intensity and *E. coli* initial concentration (10^4 CFU·mL^{-1} and 10^6 CFU·mL^{-1}). The initial concentrations of the rest of species were set as 20 nM of H_2O_2 [33], 20 μM of SOD [33] and 92 μM of CAT [31,32], referred to the bacterial cell volume.

The expressions of the reaction rates for all the species are shown in Table 1. The bacterial inactivation reaction (R1) is referred to the water volume whereas the concentration of CAT, SOD and H_2O_2 species are referred to the bacterial cell volume. Therefore, these concentrations were corrected with the ratio between the cell volume and total volume before introducing them into the kinetic expressions. Moreover, the expressions have to be also modified to include them in the units required by ANSYS® Fluent (kmol·m^{-3}·s^{-1}).

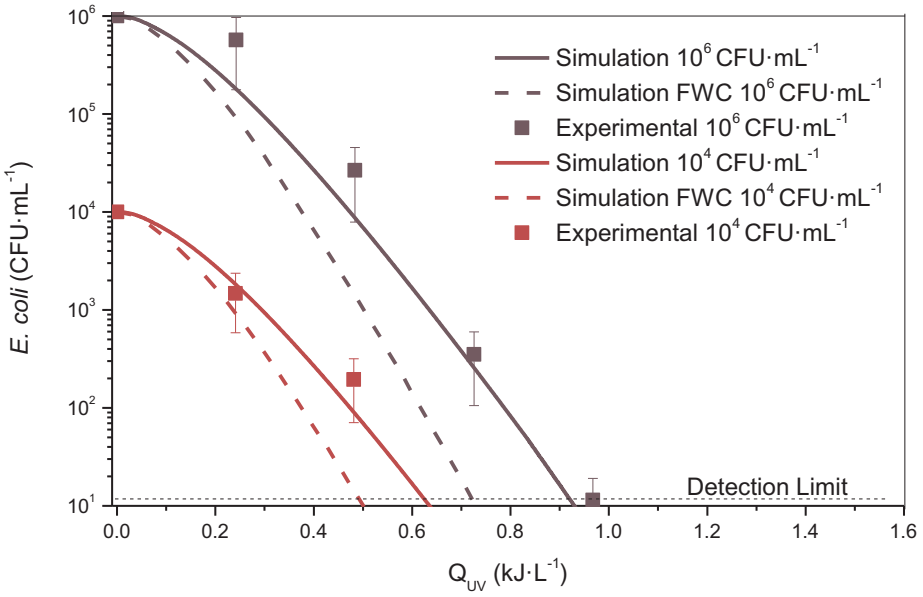

Fig. 11. Comparison of experimental results and simulation for model validation under natural solar light. Continuous line corresponds to the simulation using the experimental irradiance values. Dashed line corresponds to the simulation using the irradiance predicted by the FWC model. Experiment were carried out the 30th August (10^6 CFU·mL^{-1}) and 31st August (10^4 CFU·mL^{-1}) at Rey Juan Carlos University (Latitude 40.3° N and Longitude 3.86° W.

Finally, recirculation was simulated through a UDF taking into account the dilution effect of the outlet concentration of the photoreactor in the reservoir tank according to Eq. (10).

$$Y_i = \frac{Y_{i\,out}\cdot\Delta t + ST\cdot Y_{i\,in}}{\Delta t + ST} \quad (10)$$

where Y_i is the inlet mass fraction of species every time step; ST is the space time in the reservoir tank (2.98 s); and Δt is the time step (1 s).

3.6. Convergence criteria and solution strategy

Second order upwind discretization scheme was used to solve the equations of mass conservation and first order upwind discretization was used for hydrodynamics and DOM equations. Results of hydrodynamics and DOM solved with first order upwind were compared with the results solved with second order upwind and the differences were in both cases below 1%. Thus, the first order upwind was selected to optimize computational time. The SIMPLE algorithm was used for the pressure–velocity coupling. The simulations were carried out using the double-precision solver and with standard values of the under-relaxation factors due to good convergence and reasonable computational time. Scaled residuals of the numerical solution were monitored, considering that the equations converged when residuals achieved a value of 10^{-6} for continuity, momentum variables and incident radiation, and 10^{-4} for the concentrations. Furthermore, the variables of interest were monitored at different surfaces and volumes as an additional indicator of convergence (at least 50 iterations with stable values).

4. Results and discussion

4.1. Hydrodynamics

For the simulation of the fluid flow and the velocity field along the tubular photoreactor, it is important to consider that the fluid enters the photoreactor from a pipe that connects it with the reservoir tank, with a change in the pipe section. Therefore, the flow is developing along the reactor length (Fig. 2), with a more pronounced velocity gradient and higher fluid velocity in the center of the pipe as the fluid moves forward in the tube.

The calculated velocity profile has been compared with the theoretical velocity profile of fully developed flow calculated using Karman equations [38]. For an inlet velocity of 0.39 $m\cdot s^{-1}$ and a diameter of 26 mm, Fig. 3 shows the comparison between the numerical results of the simulation at the cross sections represented in Fig. 2 and the theoretical velocity profile. It is confirmed how the flow develops along the tube reaching a fully developed flow close to the reactor outlet.

4.2. Radiation distribution

Figs. 4 and 5 show the distribution of direct radiation within the reflector and tubular reactor for a incident light perpendicular to the *collection area* (Fig. 4) and with an angle of 45° (Fig. 5). Similar results are obtained for other directions and diffuse radiation. It is confirmed how the radiation incident to the aluminium surface of the CPC is mainly reflected towards the tubular reactor in the axis, being the radiation maps in agreement with the results previously reported by other authors by ray tracing techniques [39,40]. As it is shown, the design of the CPC with an acceptance angle of 180° allows the collection and reflection to the tubular photoreactor of the incident radiation independently of its direction. Although the use of a higher concentration factor would be beneficial for the disinfection process due to the increase in the temperature, the use of non-concentration collector makes possible the operation of the system with diffuse solar light, which, depending on the weather conditions, can represent a significant fraction of the total solar irradiance.

Experimental validation of the model predictions has been also carried out by means of actinometrical measurements with experiments under controlled irradiance in the *collection area* using the solar simulator. Table 2 compares the values of the average incident radiation in the reactor calculated from the simulations and the values of the actinometrical runs (with their experimental errors). As it can be seen, the model was able to predict accurately the incident radiation in the reactor.

The estimation of the radiation distribution as a function of the angle of the incident natural sunlight can be easily performed by coupling the calculation of the solar vector with the solution of the radiation transport by the DOM. Fig. 6 shows the contours of incident radiation in the photoreactor for different inclination angles of the CPC and the solar vector and irradiance corresponding to the solar noon of summer and winter solstices at Móstoles, Spain (40.33°N, 3.86°W). As expected, the optimal inclination to maximize the performance of the collector along the whole year corresponds to the angle of the local latitude with the *collection area* facing the Equator.

It can be seen that on the summer solstice, the horizontal position and the 40° inclination position lead to the highest values of the incident radiation, with radiation fluxes through the *collection area* ranging from 39.0 $W\cdot m^{-2}$ (horizontal) to 37.5 $W\cdot m^{-2}$ (40° inclination position) while only 11.8 $W\cdot m^{-2}$ are collected in the vertical position. An average incident radiation of 108.0 $W\cdot m^{-2}$ is concentrated in the photo reactor in the horizontal position, decreasing to 104.9 $W\cdot m^{-2}$ when the reactor is angled 40° from the horizontal, and to only 42.6 $W\cdot m^{-2}$ if the CPC is placed vertically. The opposite effect occurs near the winter solstice. The reactor oriented vertically and with a 40° inclination maximizes the incident radiation. In this case, the UV irradiances at the *collection area* are slightly lower, from 34.8 $W\cdot m^{-2}$ with 40° of inclination to 35.5 $W\cdot m^{-2}$ vertically and only 17.2 $W\cdot m^{-2}$ in horizontally. This results in values of the average incident radiation in the photo reactor of 96.3, 98.1 and 56.6 $W\cdot m^{-2}$, for the CPC placed vertically, at 40°, and horizontally, respectively. As expected, the inclination of 40° allows a more constant irradiance in the reactor throughout the year.

Beside this, simulations were performed by varying the time of day with the reactor facing south towards the equator and with an inclination angle of 40°. Fig. 7 shows the result of the incidence of the sun radiation on the reactor along on 21st of June (top) and on 21st of December (bottom). At 8:30 a.m. in June, when the sun rises in the East, the radiation is incident in the left side of the reactor with a 1.4 $W\cdot m^{-2}$ of UV intensity while in December the sun is hidden yet. The maximum irradiance is reached at the solar noon, and as the sun moves westward, radiation is incident in the right side of the reactor. Although the maximum values of UV intensity are very similar in both dates (37.4 $W\cdot m^{-2}$ in June and 34.4 $W\cdot m^{-2}$ in December at 2 p.m.), the total solar UV energy cumulative during the whole is significantly higher in June, due to the longer daylight time.

The solar vector and therefore the solar irradiance, is also strongly variable with the latitude on the Earth's surface, what makes the UV dose, and consequently the required SODIS exposure time, very dependent on the geographical coordinates. Fig. 8 shows the UV irradiance at the solar noon of the summer and winter solstices at five selected Earth locations, two in the Northern Hemisphere (one in the tropical region), one close to the Equator and two in the Southern Hemisphere (one in the tropical region). In all cases, the CPC collector was placed facing the Equator with an inclination angle corresponding to the local latitude, and the radiation incident to the *collection area* was estimated with the FWC method. It can be observed how the contour plots in Fig. 8 do not show shadow regions, because they are placed with the optimal inclination. The quantitative results confirm how on the 21st June, the incident radiation reaching the reactor is higher in the CPC placed in the Northern Hemisphere locations, whereas locations in the Southern Hemisphere receive more radiation on the 21st December, corresponding to the time of the year when the solar light is more perpendicular to the Earth's surface at each region. For example, the photoreactor placed in Madrid (latitude 40.3°N) receives an average

incident radiation of 104.9 W·m^{-2} in June and 98.1 W·m^{-2} in December, whereas the photoreactor of Stellenbosch (latitude 34.0°S) presents average values of 88.7 W·m^{-2} in June and 117.3 W·m^{-2} in December. Nevertheless, it is remarkable how the use of the optimal inclination leads to minor differences in the maximum value of irradiance along the year for each specific location, although again the total UV energy cumulative during the whole day will change significantly along the year.

4.3. Bacterial inactivation rate

Once the available radiation in the photoreactor is known, the bacterial inactivation performance as a function of the solar exposure time can be predicted. To this aim, the mass balances of the viable and inactivated bacteria and those of CAT, SOD and NADH species have to be solved, being the reaction rate coupled to the radiation field through the values of the local volumetric rate of photon absorption that appears in the kinetic expression of Table 1. Experiments using simulated solar radiation with different intensities were carried out in order to validate the global procedure proposed for modeling of CPC photoreactors. Three UV radiation intensities provided by the xenon lamp were used, corresponding to irradiance values in the *collection area* of 15.7, 21.7 and 24.8 W·m^{-2}. Fig. 9 shows the distribution of viable *E. coli* inside the photoreactor in a certain time step. It can be observed how the concentration decreases along the tube length and is also lower close to the reactor wall, where the velocity is lower, and especially in the bottom part where the radiation is higher.

The comparison of the experimental data with the predicted results provided by the simulation model is showed in Fig. 10. As expected, for the same initial bacterial concentration, the exposure time required for a complete disinfection decreases for higher UV radiation intensity. Deviations of the model predictions were quantified by the *normalized root mean squared logarithmic error* (NRMSLE), according to equation Eq. (11):

$$NRMSLE = \frac{\sqrt{\frac{1}{n}\sum_i^n [[\log(m_i+1)-\log(e_i+1)]^2]}}{\frac{\sum_i^n \log(e_i)}{n}}\cdot 100 \quad (11)$$

where n is the number of experimental points, m is the predicted value and e the experimental value of viable bacteria concentration.

The prediction of the solar disinfection model shows a good agreement with the experimental data with NRMSLE values of 3.39%, 10.2% and 6.41% for the experiments with UV irradiances of 15.7, 21.7 and 24.8 W·m^{-2}, respectively.

Regarding the use of natural sunlight, two different experiments with difference *E. coli* initial concentration of 10^6 CFU·mL^{-1} and 10^4 CFU·mL^{-1} were performed on the 30th and 31st August. Simulations of the numerical model were carried out in two different ways: i) using the theoretical value of irradiance calculated by the FWC model (39.1 W·m^{-2} in both cases); and, ii) using the average irradiance values measured by radiometry during the experimental runs (24.4 and 24.3 W·m^{-2}, respectively). In both cases, the solar vector was provided by the *solar calculator* tool. As expected from the differences in the irradiance values, the simulation of the bacterial inactivation process with both approaches led to significantly different predictions (Fig. 11). The inactivation predicted with the experimental irradiance values leads to concentrations of viable *E. coli* considerably more accurate with regards to the experimental data, with NRMSLE values of 10.0% and 9.4% for the experiments with initial concentrations of 10^6 and 10^4 CFU·mL^{-1}, respectively. In contrast, the predictions with the FWC method led to a significant overestimation of the inactivation process, with values of NRMSLE of 44.1% and 46.2%, respectively. A possible way to improve the prediction of the FWC method is including a cloudiness factor to decrease the theoretical irradiance. The theoretical incident radiation values reported by the model differ from the measurements because the model does not automatically consider the effect of clouds on available radiation. Based on the experimental value of the incident radiation, the value of the cloudiness factor estimated by trial and error for these specific days was 0.57. This value is probably too high to be understood with physical meaning, and it should be considered only as a correction factor.

5. Conclusions

The multiphysics modelling of the SODIS process has been proved to be a powerful tool for the simulation and prediction of the performance of the solar disinfection of water, allowing an accurate prediction of photoreactor behavior.

The coupling of the calculation of the theoretical solar vector and irradiance with the solution of the radiation transport allows the model to predict the required solar exposure time at any specific location on the Earth's surface and for any date and time.

The use of a mechanistic kinetic model of the bacterial inactivation process allows the coupling of the mass balance of viable and inactivated bacteria with the local volumetric rate of photon absorption calculated by the solution of the radiative transfer equation.

Finally, the experimental validation of the model predictions using bacterial inactivation data measured in a tubular photoreactor coupled with a CPC using both simulated solar light and natural sunlight (with different irradiances and initial concentration of bacteria) confirms the relevance of the developed simulation tool for the enhancement and optimization of scaled-up SODIS processes.

Acknowledgements

The authors gratefully acknowledge the financial support of the European Union's Horizon 2020 research and innovation programme in the frame of the WATERSPOUTT H2020-Water-5c-2015 project (GA 688928). Ángela Garcia Gil also acknowledges Técnicas Reunidas for the economic support in order to finance her scholarship in Residencia de Estudiantes.

References

[1] M. Sommer, B. Mariño, A. Solarte, Y. Salas, M.L. Dierolf, C. Valiente, C. Mora, D. Rechsteiner, R. Setter, P. Wirojanagud, W. Ajarmeh, H. Al-Hassan, A. Wegelin, SODIS-an emerging water treatment process, Water Supply Res. Technol. 46 (1997) 127–137.

[2] K.G. McGuigan, R.M. Conroy, H.-J. Mosler, M. du Preez, E. Ubomba-Jaswa, P. Fernandez-Ibañez, Solar water disinfection (SODIS): A review from bench-top to roof-top, J. Hazard. Mater. 235 (2012) 29–46.

[3] EAWAG, Solar Water Disinfection, The Method. (2017). http://www.sodis.ch/methode/index_EN (accessed May 28, 2018).

[4] D.M.A. Alrousan, M.I. Polo-López, P.S.M. Dunlop, P. Fernández-Ibáñez, J.A. Byrne, Solar photocatalytic disinfection of water with immobilised titanium dioxide in recirculating flow CPC reactors, Appl. Catal., B 128 (2012) 126–134.

[5] S. Malato, P. Fernández-Ibáñez, M.I. Maldonado, J. Blanco, W. Gernjak, Decontamination and disinfection of water by solar photocatalysis: Recent overview and trends, Catal. Today. 147 (2009) 1–59.

[6] F. Colina-Márquez, Jose A. López-Vásquez, Andrés F. Machuca-Martínez, Modeling of direct solar radiation in a compound parabolic collector (CPC) with the ray tracing technique, DYNA 77 (2010) 132–140.

[7] C. Navntoft, E. Ubomba-Jaswa, K.G. McGuigan, P. Fernández-Ibáñez, Effectiveness of solar disinfection using batch reactors with non-imaging aluminium reflectors under real conditions: natural well-water and solar light, J. Photochem. Photobiol. B 93 (2008) 155–161.

[8] S. Malato Rodríguez, J. Blanco Gálvez, M.I. Maldonado Rubio, P. Fernández Ibáñez, D. Alarcón Padilla, M. Collares Pereira, J. Farinha Mendes, J. Correia de Oliveira, Engineering of solar photocatalytic collectors, Sol. Energy 77 (2004) 513–524.

[9] I. Salgado-Tránsito, A.E. Jiménez-González, M.L. Ramón-García, C.A. Pineda-Arellano, C.A. Estrada-Gasca, Design of a novel CPC collector for the photodegradation of carbaryl pesticides as a function of the solar concentration ratio, Sol. Energy 115 (2015) 537–551.

[10] R.M. Tyrrell, S.M. Keyse, New trends in photobiology the interaction of UVA radiation with cultured cells, J. Photochem. Photobiol. B 4 (1990) 349–361.

[11] R.P. Sinha, D.-P. Häder, UV-induced DNA damage and repair: a review, Photochem. Photobiol. Sci. 1 (2002) 225–236.

[12] O.K. Dalrymple, E. Stefanakos, M.A. Trotz, D.Y. Goswami, A review of the mechanisms and modeling of photocatalytic disinfection, Appl. Catal., B 98 (2010)

27–38.
[13] M. Castro-Alférez, M.I. Polo-López, J. Marugán, P. Fernández-Ibáñez, Mechanistic model of the *Escherichia coli* inactivation by solar disinfection based on the photo-generation of internal ROS and the photo-inactivation of enzymes: CAT and SOD, Chem. Eng. J. 318 (2017) 214–223.
[14] S. Elyasi, F. Taghipour, Simulation of UV photoreactor for water disinfection in Eulerian framework, Chem. Eng. Sci. 61 (2006) 4741–4749.
[15] Y. Boyjoo, M. Ang, V. Pareek, Some aspects of photocatalytic reactor modeling using computational fluid dynamics, Chem. Eng. Sci. 101 (2013) 764–784.
[16] M.A. Shannon, P.W. Bohn, M. Elimelech, J.G. Georgiadis, B.J. Marinas, A.M. Mayes, Science and technology for water purification in the coming decades, Nature 452 (2008) 301–310.
[17] B.A. Wols, J.A.M.H. Hofman, W.S.J. Uijttewaal, L.C. Rietveld, J.C. van Dijk, Evaluation of different disinfection calculation methods using CFD, Environ. Model. Software 25 (2010) 573–582.
[18] A. Angeloudis, T. Stoesser, R.A. Falconer, Predicting the disinfection efficiency range in chlorine contact tanks through a CFD-based approach, Water Res. 60 (2014) 118–129.
[19] J. Chen, B. Deng, C.N. Kim, Computational fluid dynamics (CFD) modeling of UV disinfection in a closed-conduit reactor, Chem. Eng. Sci. 66 (2011) 4983–4990.
[20] T. Sultan, Numerical study of the effects of lamp configuration and reactor wall roughness in an open channel water disinfection UV reactor, Chemosphere 155 (2016) 170–179.
[21] M. Antonelli, M. Francesconi, P. Di Marco, U. Desideri, Analysis of heat transfer in different CPC solar collectors: a CFD approach, Appl. Therm. Eng. 101 (2016) 479–489.
[22] M. Antonelli, A. Baccioli, M. Francesconi, R. Lensi, L. Martorano, Analysis of a low concentration solar plant with compound parabolic collectors and a rotary expander for electricity generation, Energy Procedia 45 (2014) 170–179.
[23] C. Reichl, F. Hengstberger, C. Zauner, Heat transfer mechanisms in a compound parabolic concentrator: comparison of computational fluid dynamics simulations to particle image velocimetry and local temperature measurements, Sol. Energy 97 (2013) 436–446.
[24] K.K. Philippe, R. Timmers, R. van Grieken, J. Marugán, Photocatalytic disinfection and removal of emerging pollutants from effluents of biological wastewater treatments, using a newly developed large-scale solar simulator, Ind. Eng. Chem. Res. 55 (2016) 2952–2958.
[25] J.C. Mialocq, X. Armand, S. Marguet, A new sensitive chemical actinometer for time-resolved and continuous photochemistry: the DCM styrene dye, J. Photochem. Photobiol. A 69 (1993) 351–356.
[26] N.C. Markatos, The mathematical modelling of turbulent flows, Appl. Math. Model. 10 (1986) 190–220.
[27] ANSYS®, ANSYS User and Theory Guide, Release 14.5, in: ANSYS Fluent, Cecil Townsh, 2012.
[28] T.A. Jackson, A. Karapetian, A.F. Miller, T.C. Brunold, Spectroscopic and computational studies of the azide-adduct of manganese superoxide dismutase: definitive assignment of the ligand responsible for the low-temperature thermochromism, J. Am. Chem. Soc. 126 (2004) 12477–12491.
[29] E. Nakamaru-Ogiso, M.-C. Kao, H. Chen, S.C. Sinha, T. Yagi, T. Ohnishi, The membrane subunit NuoL(ND5) is involved in the indirect proton pumping mechanism of *Escherichia coli* complex I, J. Biol. Chem. 285 (2010) 39070–39078.
[30] I. Kishko, B. Harish, V. Zayats, D. Reha, B. Tenner, D. Beri, T. Gustavsson, R. Ettrich, J. Carey, Biphasic kinetic behavior of *E. coli* WrbA, an FMN-dependent NAD(P)H:quinone oxidoreductase, PLoS One 7 (2012) e43902.
[31] L.C. Seaver, J.A. Imlay, Alkyl hydroperoxide reductase is the primary scavenger of endogenous hydrogen peroxide in *Escherichia coli*, J. Bacteriol. 183 (2001) 7173–7181.
[32] L.C. Seaver, J.A. Imlay, Hydrogen peroxide fluxes and compartmentalization inside growing *Escherichia coli*, J. Bacteriol. 183 (2001) 7182–7189.
[33] J.A. Imlay, Cellular defenses against superoxide and hydrogen peroxide, Annu. Rev. Biochem. 77 (2008) 755–776.
[34] National Renewable Energy Laboratory, Solar Position Algorithm| NREL, (n.d.). Available from: http://www.nrel.gov/mide/solpos.spa.html.
[35] ASHRAE Handbook, Fundamentals, American Society of Heating, Refrigerating and Air-Conditioning Engineers Inc., Atlanta, 2001.
[36] R.E. Bird, R.L. Hulstrom, L.J. Lewis, Terrestrial solar spectral data sets, Sol. Energy. 30 (1983) 563–573.
[37] R.M. Ford, R.W. Harvey, Role of chemotaxis in the transport of bacteria through saturated porous media, Adv. Water Resour. 30 (2007) 1608–1617.
[38] R. Byron Bird, W.E. Stewart, E.N. Lightfoot, Transport Phenomena, John Wiley & Sons, New York, 2004.
[39] D. Robert, S. Malato, Solar photocatalysis: a clean process for water detoxification, Sci. Total Environ. 291 (2002) 85–97.
[40] J. Marugán, M.J. López-Muñoz, P. Fernández-Ibáñez, S. Malato, Solar photocatalysis: fundamentals, reactors and applications, in: D.D. Dionysiou, G. Li Puma, J. Ye, J. Schneider, D. Bahnemann (Eds.), Photocatal. Appl. Royal Society of Chemistry, Croydon, 2016, pp. 92–129.